PCCP

Accepted Manuscript

Journal Name

ARTICLE TYPE

Mesoscopic Modeling of Li Insertion in Phase-Separating Electrode Materials: Application to Lithium Iron Phosphate

Mohammad Farkhondeh[a], Mark Pritzker[a]*, Michael Fowler[a], Mohammadhosein Safari[b], Charles Delacourt[c]*

A simple mesoscopic model is presented which accounts for the inhomogeneity of physical properties and bi-stable nature of phase-change insertion materials used in battery electrodes. The model does not include any geometric detail of the active material and discretizes the total active material domain into
10 meso-scale units featuring basic thermodynamic (non-monotonic equilibrium potential as a function of Li content) and kinetic (insertion/de-insertion resistance) properties. With only these two factors incorporated, the model is able to simultaneously capture unique phenomena including the memory effect observed in lithium iron phosphate electrodes. The analysis offers a new physical insight into modeling of phase-change active materials which are of special interest for use in high power Li-ion batteries.

15 1   Introduction

$LiFePO_4$ (LFP) has recently emerged as a suitable positive electrode material for Li-ion batteries due to its durability, low cost and minimal environmental impact.[1,2] Due to a series of improvements such as reduction of particle size to nano scale[3,4]
20 and the application of coatings with high electronic[5,6] and ionic conductivity[7] onto their surfaces, LFP has become an outstanding cathode material for use in high-power Li-ion batteries.

Lithiation/delithiation of LFP occurs through a biphasic insertion reaction between Li-rich $Li_{1-\varepsilon}FePO_4$ and Li-poor
25 $Li_{\varepsilon}FePO_4$ end-members[1,8] (ε and $\varepsilon'<<1$) which have the same crystal structure (*Pnma* space group) but differ in their Li content and lattice parameters.[1] The phase transformation is characterized by an equilibrium potential that does not vary with the electrode state-of-charge (SOC). Conventional continuum
30 models describe this phase transformation by juxtaposing the two phases within the bulk throughout the charge/discharge process[9-27]; the formed phase boundary, either sharp or diffuse, travels across the material at a rate closely proportional to the charge/discharge rate of the electrode. A group of these models
35 depicts the electrochemically-driven phase transition using statistical nucleation and growth formulations such as the Kolmorogov-Johnson-Mehl-Avrami (KJMA) model.[23-25] A second group including the reformulated phase-field models for open systems relies on the spontaneous spinodal decomposition
40 mechanism and automatically tracks the phase boundary by minimizing the Cahn-Hilliard free energy functional.[9,10,15,16,18-22] By implementing an anisotropic Li diffusivity, the surface-reaction-limited phase-field model[16] is able to predict 1-dimensional Li diffusion (*i.e.*, *b*-axis in *Pnma* space group) along
45 the phase boundary between the Li-rich and Li-poor end-members within a single particle, in agreement with some experimental observations.[28-30] Core-shell-type models constitute the third group of models and locate a well-defined interface between the two phases.[11-14,17,31] Some models of that group
50 attribute the phase-change kinetics to interface mobility.[11,12,12,13] Since the two phases differ in composition, diffusion processes are required to transport species to the reacting interface which can be limiting depending on the kinetics of the phase change. Finally, the fourth group of models describe LFP insertion as a
55 strongly nonideal solid-solution process in which the phase boundary itself is shaped on the basis of variable solid-state lithium diffusivity that goes through a minimum in the intermediate Li composition range.[26,27,32]

In contrast to the idea of the two end-members coexisting in
60 the same particle, recent phase mapping experiments on electrochemically lithiated/delithiated LFP electrodes have shown that the total Li content of the electrode is distributed between two distinct groups of particles that are either Li-rich or Li-poor.[33-36] Based on an analogy with the inflation/deflation of a
65 system of interconnected rubber balloons,[37,38] Dreyer and co-workers developed a so-called "many-particle" model where particles in a porous electrode are allowed to randomly exchange Li^+ ions and electrons through the electrolyte and the conductive matrix, respectively.[39,40] The state of the electrode evolves from a
70 given initial condition quasi-statically whereby the configurational entropy accounts for the stochastic exchange of matter among the particles. In general, whether the actual particles undergo rapid domino-cascade-like filling/extraction of

b channels or a metastable solid-solution lithiation/delithiation pathway during charge and discharge depends on the particle geometry (*i.e.*, size and shape), synthesis route, temperature and applied potential/current.[41] Dreyer's many-particle model, however, does not rely on any specific mechanism for mass transfer/phase transition within individual particles and only concludes the thermodynamics of the porous LFP electrode. Only a few continuum models in the literature consider many-particle interactions and attribute the "discrete filling" of LFP nanoparticles to porous electrode limitations[42,43] or the architecture of nanoparticulate electrodes.[44]

Aside from the flat equilibrium potential, LFP electrodes exhibit other unique features, namely: (i) outstanding rate capability,7 (ii) development of positive intensities between the X-ray diffraction (XRD) peaks of the end-members during high-rate cycling,[45,46] (iii) cycle-path dependence,[47] (iv) quasi-static potential hysteresis,[39] (v) non-monotonic current response to potential steps[25] and (vi) polarization overshoot in response to intermittent galvanostatic pulses.[26,48] The first feature has been attributed to a potential- or current-dependent alteration of the insertion mechanism from a biphasic to a single-phase solid-solution pathway in some phase-field simulations9-19 and has been addressed by introducing multiple particle bins in the core-shell,[14] resistive-reactant[49] and variable diffusivity[27] models. The second feature has been justified through a rate-dependent phase-transition pathway described in ref. 9 and 19. The third feature has been accommodated in the core-shell model by the appearance of multiple onion-like layers of Li-rich and Li-poor end members within a single particle whenever charge/discharge cycles are incomplete.[47] In the resistive-reactant model of ref. 49, this effect has been related to the existence of multiple particle bins with different electronic connectivities to the conductive matrix. The fourth feature has been explained in terms of the inter-particle communication of species in the many-particle model,[39] while the fifth has been attributed to the nucleation and growth mechanism in KJMA-based models.[23,25] In addition to these known features of LFP electrodes, Sasaki and co-workers[48] have recently reported the existence of a so-called "memory effect" for this biphasic Li insertion material. An anomalous increase in the electrode polarization is observed when the full galvanostatic charge/discharge of the LFP electrode is preceded by a partial charge/discharge cycle. They attributed this effect as well as the galvanostatic pulse polarization overshoot, to many-particle effects and hindrance associated with nucleation or spinodal decomposition within the particles.

Despite rigorous research in the literature, a single unifying model that can predict all of the above-mentioned irregularities and pinpoint the dominant contributing factors is still lacking. The current work presents a simple mesoscopic model that is able to simultaneously explain the memory effect and other unique phenomena observed in phase-transforming battery materials that have just been enumerated.

2 Model Development

The model disregards the geometric details associated with choosing between inter- and intra-particle phase-change mechanisms by defining "elementary lithiating/delithiating units" which are large enough to contain a substantial number of reaction sites and for the continuity to hold (in contrast to atomic-
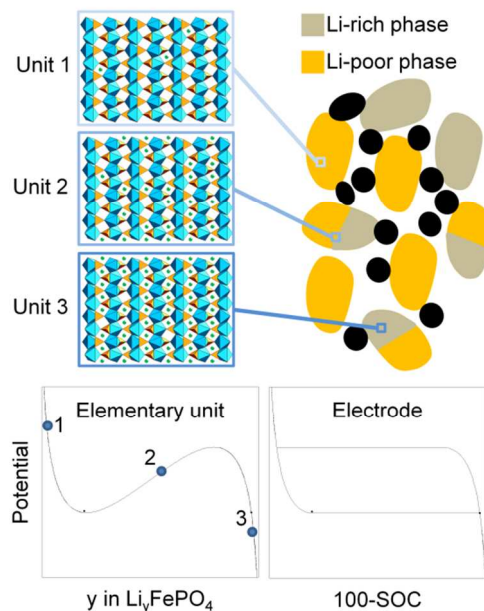
scale models), but small enough at the scale of the bulk so that no intra-unit phase transition occurs (Fig. 1). These mesoscopic units constitute the total active material loading of the electrode and may be interpreted as single Li channels lying along the *b*-axis, crystallites within a polycrystalline particle or even nanoparticles in a nanoparticulate porous electrode. An elementary unit is the smallest entity that can exchange species with its counterparts through the surrounding electronic and ionic conduits and its length scale may be defined according to the type of LFP particles making up the electrode. Such mesoscopic units resemble bi-stable elements in Preisach magnetization models or in homogenized energy models developed earlier for smart materials.[50] The term "unit" is used throughout this manuscript for notional convenience. The mathematical setting presented is deliberately kept simple and includes only the constituents necessary for demonstrating many-unit effects and avoids the description of phenomena that are already known in a porous battery electrode. Thus, the following main assumptions are made: i) chemical potential of Li in each unit is a non-monotonic function of composition, ii) units are lithiated/delithiated homogeneously, *i.e.*, mass transfer limitations are not included, iii) possible mechanical effects are ignored, iv) a distribution of resistances exists among the units and v) porous-electrode effects are ignored.

In the simplest approximation, the dependence of the single-unit equilibrium potential U_k on its composition y_k can be derived from the regular solution model for a binary system containing occupied and vacant Li sites (one-parameter Margules activity-coefficient model):

$$U_k = U^0 + \frac{gRT}{F}\left(y_k - \frac{1}{2}\right) + \frac{RT}{F}\ln\left(\frac{1-y_k}{y_k}\right), \quad (1)$$

where subscript $k \in \{1, 2,\ldots, N\}$ denotes a specific bin containing elementary units with similar properties, U^0 is the standard equilibrium potential, R is the universal gas constant, T is the temperature and F is the Faraday constant. The second term on the right side of eqn (1) is associated with the enthalpy of mixing of the inserted Li atoms and Li vacancies in the solution which can be zero ($g = 0$ in an ideal solution), negative ($g < 0$, repulsion of like neighbors) or positive ($g > 0$, attraction of like neighbors). The significant attraction of like neighbors (*i.e.*, $g > 4$) causes single-phase instability over the intermediate composition range and eventually leads to a non-monotonic dependence of the equilibrium potential on the lithium concentration. In brief, the interaction coefficient determines the extent to which the inserted Li atoms and vacancies are miscible. A similar thermodynamic model was employed in the many-particle model developed in ref. 39 and 40.

The overpotential experienced by lithiating/delithiating units is assumed to arise from an ohmic hindrance R_k (in Ω mol) that impedes the insertion/de-insertion reaction and is specific to each bin:

$$\Phi - U_k = R_k i_k, \quad (2)$$

where Φ is the electrode potential and i_k is the partial current per mole of active material in bin k and is negative when the bin is being lithiated. It should be emphasized that, according to assumption (v) above, all units are connected to an isopotential source/sink of electrons (conductive matrix) and Li ions (electrolyte). This is a reasonable assumption if the porous electrode is sufficiently thin and dilute in terms of active material loading. Assuming a uniform Li concentration within a unit, the partial currents contributed by this unit is related to the change of the Li concentration in the bin through a simple material balance expression:

$$i_k = -F\frac{\partial y_k}{\partial t}. \quad (3)$$

The assumption of a uniform concentration within each unit is not too unrealistic given that recent experiments on electrochemical[7,51] and non-electrochemical (gas phase)[52] delithiation of LFP have revealed that Li transport within LFP particles is ultrafast, with a Fickian diffusion coefficient of $\sim 10^{-9}$ to 10^{-11} cm^2 s^{-1} that agrees well with earlier theoretical calculations ($\sim 10^{-8}$ cm^2 s^{-1}).[53,54]

The total current density I applied to the electrode is related to the partial molar currents i_k entering/leaving the parallel bins as follows:

$$I = c_{max} L \varepsilon_t \sum_{k=1}^{N} \varepsilon_k i_k, \quad (4)$$

where L is the electrode thickness, ε_t is the total active material volume fraction in the electrode, ε_k is the fraction of active

material in bin k and c_{max} is the maximum lithium concentration in the active material (assumed constant since volume changes associated with lithiation/delithiation are ignored). No assumption concerning the unit geometry is made in the model. No transport limitation inside the units is considered and the model only accounts for the ohmic limitations of active material. The resistance varies from R_{min} for units in bin 1 all the way to R_{max} for units in bin N, according to the following expression:

$$R_k = \frac{1}{N-1}(R_{max} - R_{min})(k-1) + R_{min}, \quad (5)$$

and volume fractions of the bins of units are assumed to follow a Gaussian distribution:

$$\varepsilon_k = \frac{\frac{1}{S\sqrt{2\pi}}\exp\left(\frac{-(R_k - \overline{R})^2}{2S^2}\right)}{\sum_{k=1}^{N}\frac{1}{S\sqrt{2\pi}}\exp\left(\frac{-(R_k - \overline{R})^2}{2S^2}\right)}, \quad (6)$$

where S is the standard deviation and $\overline{R}$ is the mean resistance, *i.e.*, $\overline{R} = (R_{min} + R_{max})/2$. This resistance distribution represents a non-uniform physico-chemical property within the LFP electrode. In an electrode where LFP particles are large enough so that they contain a number of units, the distribution reflects that inner units are surrounded by units only whereas outer ones are partially surrounded by electrolyte. In an LFP electrode where units feature LFP nanoparticles, the distribution is in line with earlier resistive-reactant models[17,49] which rely on the poor electronic conductivity of LFP.

3   Results and Discussion

The model parameters used in this study are listed in Table 1. The values of L, ε_t and c_{max} correspond to a sample LFP electrode with a total capacity of 2.05 mAh and geometric area of 1.2 cm^{-2} studied earlier.[27] The interaction coefficient g is fitted so that the predictions of the model presented here match the experimental data in ref. 39 under pseudo-static conditions. U^0, R_{min}, R_{max} and S are estimated so that the simulations match the experimental charge/discharge curves at C/2 reported by Sasaki *et al.*[48]

Table 1 Parameters used in the model.

Parameters	Symbol	Value
Number of elementary-unit bins	N	100[a]
Minimum resistance [Ω mol]	R_{min}	6.08 10^{-5f}
Maximum resistance [Ω mol]	R_{max}	6.08 10^{-3f}
Standard deviation [Ω mol]	S	1.28 10^{-3f}
Standard equilibrium potential [V *vs*. Li]	U^0	3.427^f
Interaction coefficient in the Margules model	g	6^f
Electrode thickness [m]	L	80 10^{-6l}
Total active-material volume fraction	ε_t	0.351^l
Maximum solid-phase Li concentration [mol m^{-3}]	c_{max}	22 806^l

[a] assumed; [f] fitted; [l] literature ref. 27.

Whereas the original many-particle model was limited to

quasi-static operation,[39,40] the present model is used for both low- and high-rate conditions, while disregarding transport limitations

at the unit and electrode scales for the sake of simplicity. As shown in Fig. 2a, the model is able to predict the wide potential
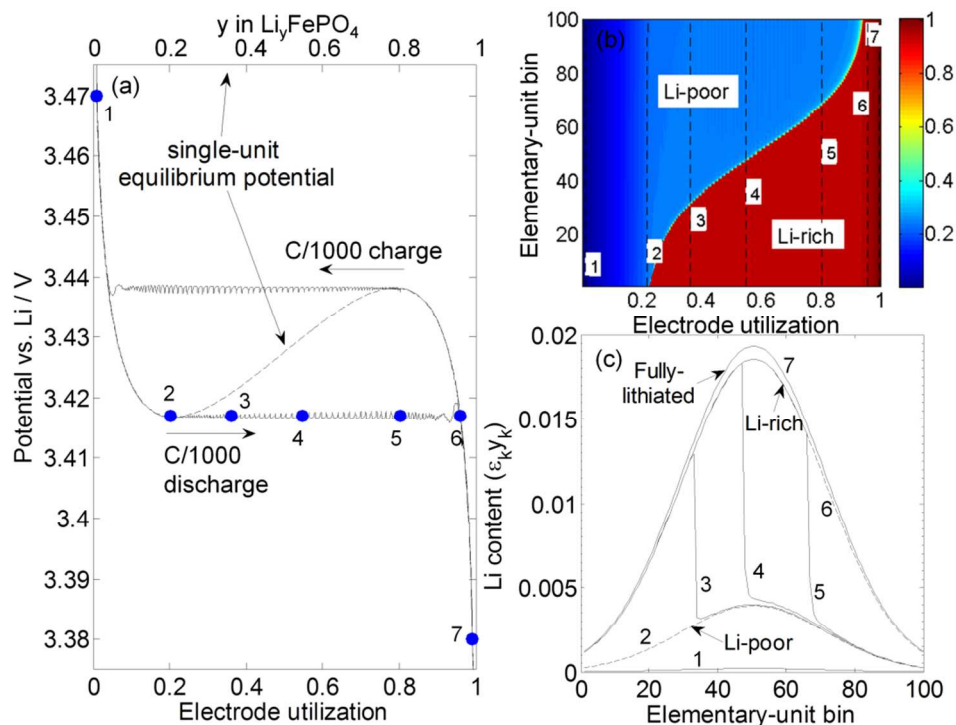

Fig. 2 (a) Voltage profile of the many-unit electrode undergoing slow galvanostatic charge/discharge (C/1000, quasi-static) compared with the single-unit equilibrium potential. (b) Bin utilization versus electrode utilization during C/1000 discharge. Numbers 1 to 7 correspond to the blue points indicated in (a). (c) Lithium content of each bin at different times during C/1000 discharge.

plateau that is typically observed for both charge and discharge potential-composition curves of two-phase battery materials. In the case shown, a very low rate (C/1000) is considered to galvanostatically charge and discharge an LFP electrode. Points labeled from 1 to 7 correspond to the results obtained over a time sequence during the C/1000 discharge. Also, the simulated curves exhibit hysteresis whereby the plateaus appear at different potentials during charging and discharging without resorting to any consideration of coherency strain energy,[55] in agreement with experimental observations and simulation results from a previous many-particle model.[39] The single-unit equilibrium potential is also included in Fig. 2a for comparison. Fig. 2b shows the dynamics of quasi-static electrode lithiation. The bin utilization is color-coded from deep blue for fully-delithiated to dark red for fully-lithiated states. Based on the model, units accommodate either the Li-poor phase or Li-rich phase at any given time and only a few bins (*e.g.*, only 1 or 2) have intermediate concentration (*i.e.*, energetically unstable) corresponding to the narrow boundary between the two regions. In other words, units are segregated into two groups, one being Li-rich and the other being Li-poor and the lithiation process occurs in a "unit-by-unit" sequence. The narrow boundary indicates that lithiation proceeds

as a distinct reaction front propagating among units during the electrode discharge. The numbered lines correspond to the numbered points on the discharge curve in Fig. 2a. The reaction front is expanded in Fig. 2c in terms of the Li content of each bin at the indicated times. At the start of discharge, units are filled together at the same rate (C/1000) while maintaining an identical Li concentration (*i.e.*, solid-solution domain) until a point is reached where even a small change of Li concentration in one unit moves it into the unstable region. This, in turn, triggers the fast traverse of the unit content across the mid-composition range, which is not energetically favorable (*i.e.*, adequate driving force $\Phi - U_k(y_k)$), to the Li-rich branch of the single-unit equilibrium potential. The process starts from the least resistive unit and ends with the most resistive one. Since all units are electronically and ionically connected, they experience the same electric potential Φ throughout the lithiation process. In the case of quasi-static operation, this potential remains almost identical to the single-unit equilibrium potential of the lower spinodal node (*i.e.*, U_k where $\partial U_k/\partial y_k = 0$) until the last unit leaves the spinodal node and crosses the unstable region. The fluctuations in the electrode potential observed along both the discharge and charge plateaus in the simulated potential-utilization curves are artifacts of the
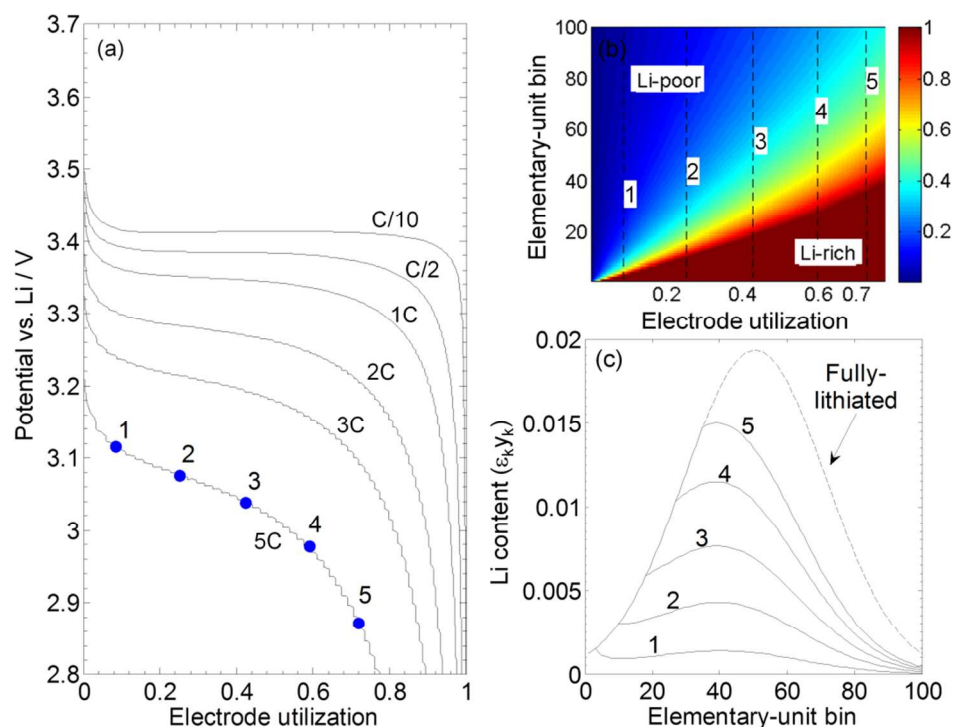
Journal Name

ARTICLE TYPE

Fig. 3 (a) Galvanostatic discharge curves at different C-rates. (b) Bin utilization versus electrode utilization during discharge at 5C. Numbers 1 to 5 correspond to the blue points indicated in (a). (c) Li content of units in each bin at different times during discharge at 5C.

model since they are caused by the sequential filling of the bins. These fluctuations are expected to smooth out and eventually vanish if the resistance is distributed across a larger number of bins (*i.e.*, continuum limit).

With an increase in the applied current, Φ deviates significantly from the spinodal node potential and enough driving force is now provided for all units to participate in charge transfer to an extent that is governed by their resistances. Consequently, the lithiation mechanism moves from a purely sequential unit-by-unit mechanism to a mixed sequential-parallel regime at high-rate charge/discharge. This change in the lithiation mechanism with applied current is demonstrated in Fig. 3b and c where a much wider range of bin utilizations between Li-rich and Li-poor states is observed than is found in the quasi-static condition in Fig. 2b. Along with the presumed fast Li transport inside the units, this effect can explain the outstanding rate capability (end-capacity as a function of applied current) of LFP electrodes. This is in line with the apparent dependence of particle size or rate constant on applied current in the single-particle analyses of ref. 56 and 49 where lower apparent particle radius or greater rate constant is required, respectively, at high current for model simulations to agree with experiments. The increase in the population of simultaneously lithiating bins at high rates agrees qualitatively

with the change of the insertion mechanism from a two-phase to a solid-solution pathway that was inferred from the development of positive intensities between the $Li_{1-\varepsilon}FePO_4$ and $Li_{\varepsilon}FePO_4$ reflections during operando XRD analysis of electrodes under rapid charge/discharge cycles.[45,46] Units with lower resistance carry higher partial currents until they become fully lithiated (left branch of the curves at given snapshots in Fig. 3c) after which their partial currents drop toward zero. Since the total current would have to be accommodated by the remaining more resistive units, this would cause them to become more polarized and the cell potential to drop leading to the downward slope in the discharge curve at intermediate electrode utilization.

Intuitively, a purely parallel lithiation mechanism would be ideal and lead to the most efficient electrode operation. Such a condition would occur if the physico-chemical properties of the units as well as their ionic/electronic environment were perfectly uniform throughout the electrode. However, as discussed in the model development, this is seldom the case in an actual many-unit ensemble and leads to the limitations associated with sequential lithiation as described above. In the model presented here, the intra-unit limitations are intentionally disregarded and the ohmic resistance distribution determines the
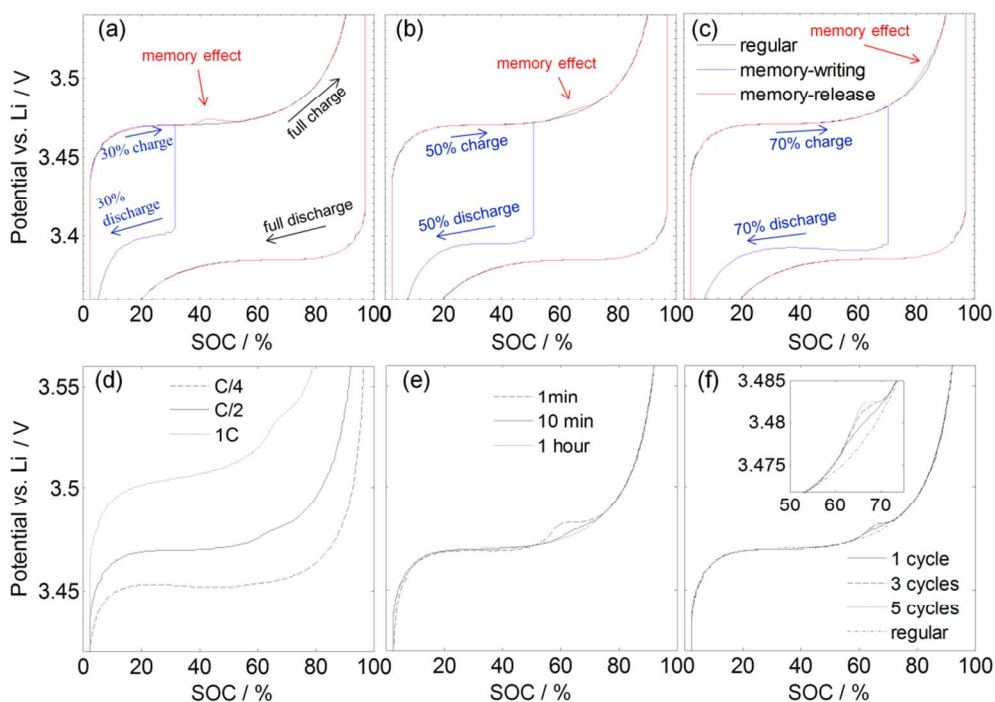
Journal Name

ARTICLE TYPE

Fig. 4 Memory effect upon (a) 30%, (b) 50% and (c) 70% partial charge-discharge memory-writing cycles, as indicated by the red arrow. Effects of (d) memory-release rate, (e) rest time between the memory-writing and memory-release cycles and (f) number of successive memory-writing cycles on the extent of the memory potential bump. The rate for both memory-writing and memory-release cycles is C/2 with 10 minutes of relaxation time between
5 the writing and release cycles, unless otherwise stated. The memory-writing cycle is 50% deep unless otherwise stated.

sloping behavior and end-capacity of the potential-capacity curves. It implies that any improvement of the resistance distribution (*i.e.*, broadness and mean value) that shifts the lithiation mechanism toward parallel dynamics will enhance the
10 electrochemical performance of the LFP electrode. A similar statement can be made for other distributed properties in an actual electrode such as unit size, single-unit equilibrium potential and/or ionic/electronic resistances across the electrode.

The memory effect in Li-ion batteries is defined as an
15 abnormal potential overshoot observed in the charge-discharge cycle immediately following a partial charge-discharge cycle.[48] The mesoscopic model presented here is used to predict the results obtained from a set of virtual experiments that mimic the actual experiments described in ref. 48. This experiment consists
20 of a sequence of 3 stages: memory-writing, memory-release and regular cycles. The initial condition is set to $y_1 = y_2 = \ldots = y_N = 0.975$ (*i.e.*, SOC = 2.5%) in the units so that the electrode is, in practice, fully discharged at the outset. Starting from this state, the electrode is first charged (at C/4, C/2 or 1C) to a certain state-
25 of-charge (30%, 50% or 70%) whereupon it is allowed to rest for 1 hour. This is followed by a discharge step that brings the

electrode back to the initial SOC (memory-writing cycle). After another rest period (1 minute, 10 minutes, or 1 hour), the electrode is fully charged (SOC = 100%) and then allowed to rest
30 for 1 hour before being discharged to the initial SOC (memory-release cycle). The third cycle is a repetition of the second one as a control to confirm the observations (regular cycle). As shown in Fig. 4a-c (compare with Fig. 2 of ref. 48 the potential bump appearing during the memory-release cycle (red line) coincides
35 with and tracks the depth of the memory-writing cycle (blue line), *i.e.*, the electrode potential remembers the depth of the previous shallow cycle. Also, fully charging of the electrode erases the memory effect and the bump is no longer observed during the subsequent charge-discharge cycles (regular cycle, black line).
40 The effects of the release cycle rate, rest time between the writing and release cycles and the repetition of multiple memory-writing cycles are presented in Fig. 4d-f, respectively. The results show that the potential anomaly is amplified by increasing the applied current during the release cycle, which stems from the resistive
45 nature of the units assumed in the model. For a writing cycle of 50% charge-50% discharge, the relaxation time inversely affects the memory effect, *i.e.*, the potential bump diminishes and
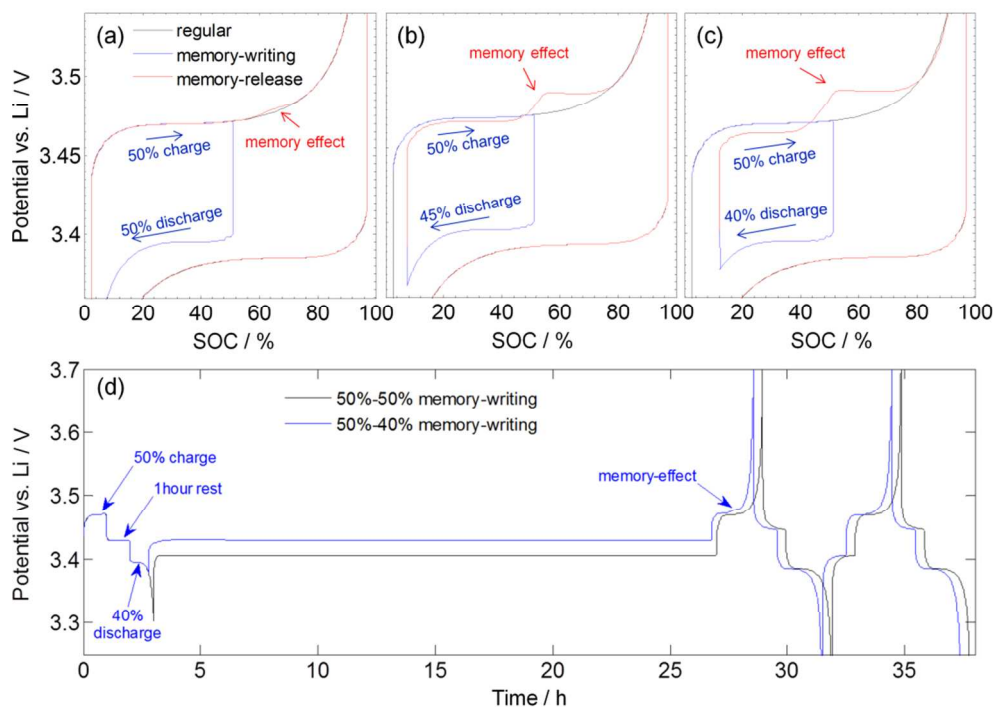
Journal Name

ARTICLE TYPE

Fig. 5 Memory effect during a charge following memory-writing cycles with 50% depth of charge and (a) 50%, (b) 45% and (c) 40% depths of discharge. (d) Effect of long relaxation time (24 h) after shallow (blue) and deep (black) memory-writing discharges. The rate during both memory-writing and memory-release cycles is C/2 with 10 minutes of ret time between the writing and release cycles, unless otherwise stated.

5 ultimately disappears as the relaxation time is increased. In addition, the memory effect is enhanced by repeating the same memory-writing cycle a number of times (Fig. 4f).

The impact of the depth-of-discharge of the memory-writing cycle is shown in Fig. 5a-c. The memory effect becomes more 10 pronounced as the depth of discharge decreases and the writing cycle becomes more imbalanced. Moreover, the potential overshoot does not disappear after a long relaxation step succeeding the 50% charge-40% discharge cycle (Fig. 5d), which contrasts with the balanced memory-writing cycle described 15 earlier (Fig. 4e). The simulation results for all of the above-mentioned operations agree qualitatively with the reported experimental results[48] in spite of the simplicity of the model, implying that the incorporation of the non-monotonic single-unit potential and the resistance distribution in the many-unit effects is 20 responsible for these observed phenomena.

In order to gain further insight into the above observations, unit utilizations are plotted in Fig. 6 at the outset and end of the steps constituting the memory-writing cycle for the selected experiments. Theoretically, a fully-discharged electrode would 25 consist of elementary units with Li concentration equal to 1; in practice, however, this is not the case and the end-capacity

deviates from the theoretical value as the applied current increases (*e.g.*, C/2, the experimental condition used by Sasaki *et al.*).[48] Therefore, the initial concentration of Li in the units is set 30 to be below 1 and within the Li-rich solid-solution region according to the single-unit equilibrium function. This also guarantees zero inter-unit exchange of species and initial stability of the electrode. Although not included here, simulations with zero initial state-of-charge did not generate any memory effect for 35 a perfectly balanced memory-writing cycle. At the same time, the results in Fig. 5 show that the memory effect becomes more pronounced as the memory-writing cycle becomes more imbalanced. Taken together, these findings indicate that a necessary condition for the memory effect to appear in an LFP 40 electrode is the existence of a non-zero residual capacity at the onset of memory-release charging which may originate either from a non-zero initial SOC or from an imbalanced writing cycle. A memory effect should therefore not be observed in an electrode that has been preconditioned at extremely low currents (*i.e.*, zero 45 initial SOC) and has undergone an extremely slow memory-writing cycle (*i.e.*, approaching a balanced cycle).

The uniform Li content initially set for all units evolves during the memory-writing charge according to the resistivity of the
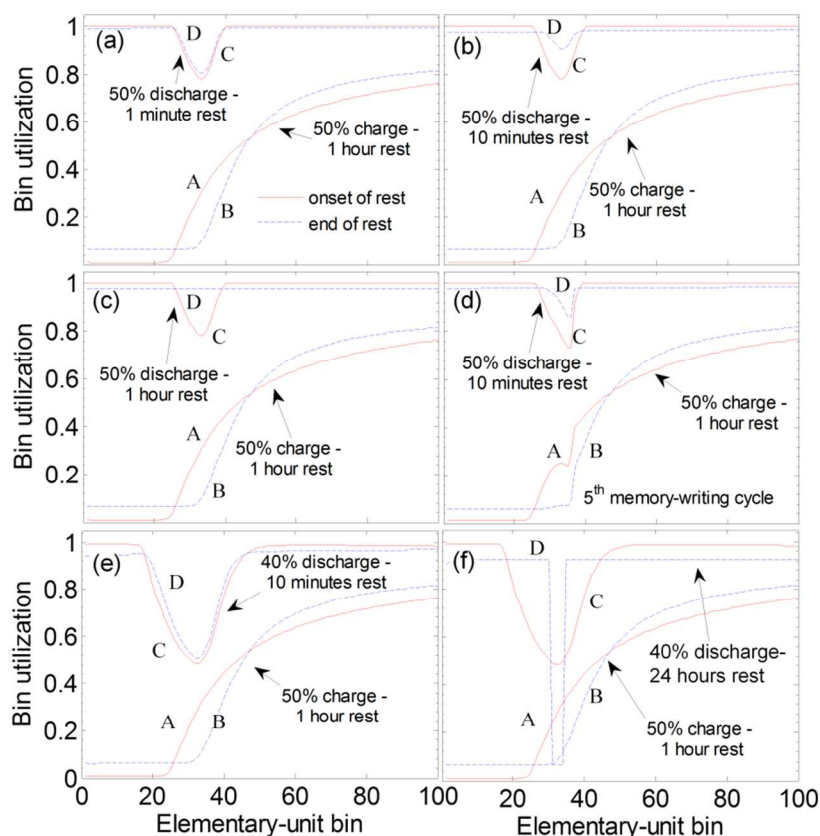
Journal Name

ARTICLE TYPE

Fig. 6 Utilization of elementary-unit bins at the outset and end of relaxations during the memory-writing cycle for the following 6 different sequences: (a) 50% charge, 1 h rest, 50% discharge, 1 min rest, (b) 50% charge, 1 h rest, 50% discharge, 10 min rest, (c) 50% charge,1 h rest, 50% discharge, 1 h rest, (d) 5 cycles of 50% charge, 1 h rest, 50% discharge, 10 min rest, (e) 50% charge, 1 h rest, 40% discharge, 10 min rest and (f) 50% charge, 1 h rest, 40% discharge, 24 h rest.

units until the electrode reaches its assigned depth of charge (stage labeled A in Fig. 6a-f). The next rest period leads to a redistribution of Li among the units which may or may not reach their most stable state depending on the relaxation time (stage B). The subsequent discharge transforms both stable delithiated (least-limiting trail) and the partially-delithiated (thermodynamically unstable) units to the Li-rich phase generating an unusual utilization profile even when the electrode reaches the same initial SOC (stage C). The initial residual capacity (*i.e.*, Li deficiency $\Delta y_k = 0.025$, $k = 1, 2, \ldots , N$) is redistributed and localized as a depression in the profile over a certain fraction of units (bins 26 to 39, Stage C in Fig. 6a-c) while other units are fully lithiated. Needless to say, a larger residual capacity leads to a wider and deeper depression in the bin utilization curves as shown in Fig. 6e-f. Finally, the rest period preceding the memory-release cycle enables the units to relax to a more stable condition by exchanging their Li content with each other (stage D). The localized residual capacity at the outset of the memory-release cycle (*i.e.*, stage D) is responsible for the occurrence of the memory effect. The memory effect is boosted by enlarging the accumulated residual capacity (Fig. 5a-c) or diminished by easing the utilization non-uniformity. Fig. 6a-c show the distributions of bin utilization after 3 different rest periods (1 min, 10 min and 1 h, respectively) between the writing and release cycles corresponding to the results shown in Fig. 4e. The utilization depression clearly diminishes by increasing the relaxation time from 1 min to 1 h in agreement with the disappearance of the memory potential-bump in Fig. 4e.

If the applied current is set to zero and eqn (2) is substituted into eqn (4), the following expression for the relaxing potential is obtained:
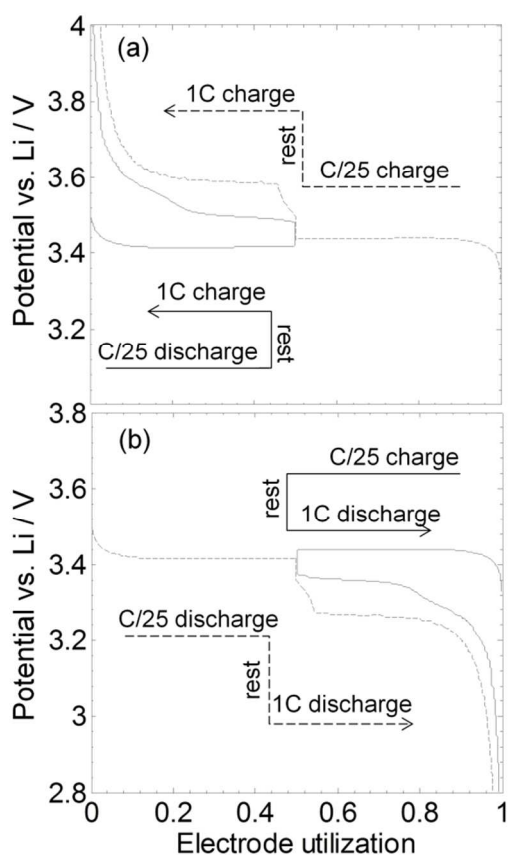
Fig. 7 Path dependence during (a) fully charging of electrode at 1C after being brought to 50% SOC at C/25 *via* different paths (charging from 0% SOC (dashed line) and discharging from 100% SOC (solid line)) and 2-h rests and (b) discharge obtained by mirroring the operating conditions in (a).

$$\Phi = \frac{\sum_{k=1}^{N} U_k(y_k) \dfrac{1}{R_k'}}{\dfrac{1}{R_{eq}}}, \qquad (7)$$

where $R_k' = R_k/\varepsilon_k$ and $1/R_{eq} = \sum_{k=1}^{N} 1/R_k'$ are the resistance of each bin and the equivalent resistance of the electrode, respectively. Based on this expression, one concludes that, given a long enough rest period, the electrode potential Φ approaches a common single-unit equilibrium potential $\overline{U(y_k)}$ for all units which may or may not correspond to a common unit utilization. For an overall electrode utilization located within the sloping branches of the electrode potential profile, a common equilibrium potential is realized only when all units share an identical Li concentration (stage D in Fig. 6c). However, if the electrode utilization is within the biphasic region, an adequate rest time causes the elementary units to segregate into two groups with an identical equilibrium potential but different Li concentrations, *i.e.*, Li-rich and Li-poor phases. Our simulations show that the equilibrium potential of the electrode ensemble is bounded within the quasi-static potential hysteresis but is not unique for a given utilization depending on the history of the electrode. Accordingly, the exact concentrations of Li in the two phases vary slightly. On

account of a non-uniform resistance, the previous history of the electrode dictates the configuration of the two phases among the units. For instance, less resistive units constitute the Li-poor phase and more resistive ones make up the Li-rich phase during a partial charge. On the other hand, after an imbalanced memory-writing cycle, the bin utilization depression grows into a gap where bins with intermediate resistivity exhibit little utilization (*i.e.*, Li-poor phase) during the relaxation (stage D in Fig. 6f). This explains why the memory effect is not removed in Fig. 5d even after a long relaxation period. Moreover, the modification of the memory effect with repetition of the same memory-writing cycle (Fig. 4f) originates from the utilization anomaly being reduced to the narrow range shown in Fig. 6d.

In order to highlight the influence of the charge/discharge history on the electrode performance, a simple path-dependence simulation is performed in accordance with the previous experiments described in ref. 49. Starting from a fully discharged state, the electrode is charged for 12.5 hours at a current density corresponding to C/25 to raise its SOC to 50%. This is followed by a 2-hour rest period after which the electrode is charged (or discharged) at 1C to 4 V (2.8 V). The same procedure is repeated in the opposite direction starting from a fully charged state; the electrode is discharged to 50% SOC over 12.5 hours at C/25 and then rested for 2 hours after which 1C discharge (or charge) current is applied until a voltage 2.8 V (4 V) is attained. Both the electrode potential and capacity differ depending on the path taken to reach the end of the charge (or discharge). The simulation results presented in Fig. 7 agree well with the trends observed experimentally and can be explained through the same reasoning discussed above for the memory effect simulations.[47,49]

An alternating sequence of constant-current and open-circuit steps constitutes the galvanostatic intermittent titration technique,[57] which is a useful method regularly employed by battery researchers to estimate the chemical diffusion coefficient of guest species in insertion materials. One distinct feature of an LFP electrode is the polarization overshoot of the applied GITT pulses compared to a continuous galvanostatic potential profile at the same current. In other words, the intermittent relaxations during the GITT pulses modify the system so as to impede the electrode response toward the subsequent pulse current. The simulations of approximate solid-solution models have not been able to show this feature. Conventional bulk phase-change models may describe it by minimizing the two-phase interface and coherency strain energies during the rest period and re-triggering the nucleation and growth process during the subsequent current pulse. The many-unit approach, on the other hand, effectively captures the GITT polarization overshoot (Fig. 8a) by allowing unstable activated units to reach their most energetically favorable configuration during intermittent rest periods, *i.e.*, either Li-rich or Li-poor phase. Considering a GITT discharge process for instance, the absence of unstable partially-lithiated units in a relaxed partially discharged electrode (*i.e.*, as opposed to an electrode at the same SOC under a continuous discharge operation) leads to a smaller number of available units (with high resistance) having to sustain the following pulse at the same current. Since this makes it more difficult for charge transfer to occur, the electrode reaches successively higher overpotentials during the subsequent pulses towards the end of
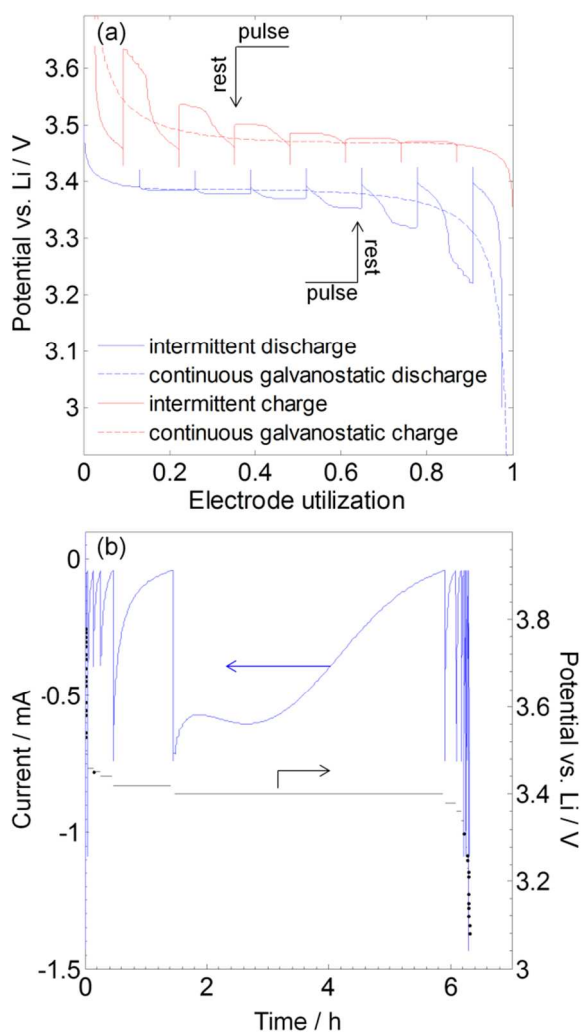
Fig. 8 (a) GITT charge and discharge (solid line) simulated by applying C/2 pulses for 16 min followed by 2 h rest. The continuous galvanostatic charge and discharge curves at C/2 (dashed lines) are included for
5 comparison. (b) PITT discharge simulated by applying the staircase potential profile with a 10 mV decrement from 3.8 to 3.0 V versus Li reference electrode. Each titration is terminated when the absolute current reaches C/50.

the discharge.

10 The potentiostatic intermittent titration technique is another electroanalytical method widely used for determining transport as well as thermodynamic properties of electrochemical materials.[58] A "staircase" voltage profile with a certain successive decrement (increment) between the upper (lower) and lower (upper) cut-off
15 potentials is applied and the current decay with time is recorded for each potential step. Each individual titration is terminated when the absolute current reaches a preset minimum value. This technique is of interest for investigating phase-change materials since it helps reveal possible phase transformation mechanisms
20 from the observed transient current (*e.g.*, KJMA analysis). More specifically, the bell-shaped current response of an LFP electrode over intermediate SOCs is commonly interpreted to arise from the nucleation and growth of the second phase[23-25,41] in contrast with the Cottrell-type current response which is indicative of a
25 diffusion-limited insertion process. However, as shown in Fig. 8b, our model is able to predict the appearance of a current hump

in the chronoamperogram although it does include the nucleation and growth of a second phase. Thus, an alternative explanation for the current hump that emerges from our model is the
30 statistical distributions of physical properties that limit the charge transfer rate in a phase-change porous electrode rather than commonly accepted phase-change mechanisms such as nucleation and growth.

The analyses presented in this manuscript help explain the
35 experimental observations[33-36,59,60] of the collective lithiation of discrete units in a porous LFP electrode. The model presented here has been evaluated under various operating modes including continuous/intermittent partial/full galvanostatic and potentiostatic cycles. Overall, the results suggest that interactions
40 among many interconnected units (*e.g.*, LiFePO$_4$) play a dominant role in the electrochemical performance of the phase-change electrode and should form the framework for a prospective comprehensive model. It is important to emphasize that the analysis in this communication has been intended for
45 demonstration purposes only. Complications at both unit (*e.g.*, charge-transfer kinetics and solid-phase electronic/ionic transport within and at the surrounding of each unit) and electrode (*e.g.*, porous-electrode effects) scales are acknowledged and should be included in such a comprehensive model for more quantitative
50 simulations.

4 Conclusions

In this communication, we have presented a simple mathematical model for the dynamics of phase-transforming porous electrodes applied to LiFePO$_4$. The model features a non-equilibrium solid-
55 solution pathway for Li insertion/de-insertion into and a Gaussian distribution of resistances among channels/crystallites/nanoparticles constituting the porous electrode. It assumes rapid transport of species inside each individual unit and an inherent distribution of physico-chemical
60 properties of the material in an ensemble of many electronically and ionically wired units. With only these two factors involved, our model can simultaneously explain a number of unique features associated with lithium iron phosphate electrochemical performance including the quasi-static potential hysteresis, high
65 rate capability, cycle-path dependence, larger electrode polarization in GITT compared with that observed during a continuous cycling at the same current, bell-shaped current response in PITT and the most recently observed memory effect. The simplicity of the model, however, does not rule out the
70 known complications at the unit and electrode levels but rather magnifies the significance of unit-to-unit interactions even at high currents and under combined operating modes which has been typically ignored in mathematical treatments of phase-change porous electrodes so far.

75 ## Notes and references

a Department of Chemical Engineering, University of Waterloo, 200 University Avenue West, Waterloo, Ontario N2L 3G1, Canada. E-mail: pritzker@uwaterloo.ca
b Department of Chemistry, University of Waterloo, 200 University
80 *Avenue West, Waterloo, Ontario N2L 3G1, Canada.*
c Laboratoire de Réactivité et de Chimie des Solides, CNRS UMR 7314, Université de Picardie Jules Verne, Amiens, France. E-mail: charles.delacourt@u-picardie.fr

1 A. K. Padhi, K. S. Nanjundaswamy and J. B. Goodenough, *J. Electrochem. Soc.*, 1997, **144**, 1188–1194.

2 *US Pat.*, 5 910 382, 1999.

3 A. Yamada, S. C. Chung and K. Hinokuma, *J. Electrochem. Soc.*, 2001, **148**, A224–A229.

4 C. Delacourt, P. Poizot, S. Levasseur and C. Masquelier, *Electrochem. Solid State Lett.*, 2006, **9**, A352–A355.

5 N. Ravet, J. B. Goodenough, S. Besner, M. Simoneau, P. Hovington and M. Armand, *196ᵗʰ Meeting of the Electrochemical Society*, 1999, **Abstract # 127 Hawai**, year.

6 N. Ravet, Y. Chouinard, J. F. Magnan, S. Besner, M. Gauthier and M. Armand, *J. Power Sources*, 2001, **97-98**, 503–507.

7 B. Kang and G. Ceder, *Nature*, 2009, **458**, 190–193.

8 A. Yamada, H. Koizumi, S.-I. Nishimura, N. Sonoyama, R. Kanno, M. Yonemura, T. Nakamura and Y. Kobayashi, *Nature Mater.*, 2006, **5**, 357–360.

9 Y.-H. Kao, M. Tang, N. Meethong, J. Bai, W. C. Carter and Y.-M. Chiang, *Chem. Mater.*, 2010, **22**, 5845–5855.

10 D. Cogswell and M. Z. Bazant, *Nano Lett.*, 2013, **13**, 3036–3041.

11 C. Wang, U. S. Kasavajjula and P. E. Arce, *J. Phys. Chem. C*, 2007, **111**, 16656–16663.

12 U. S. Kasavajjula, C. Wang and P. E. Arce, *J. Electrochem. Soc.*, 2008, **155**, A866–A874.

13 S. Dargaville and T. W. Farrell, *J. Electrochem. Soc.*, 2010, **157**, 830–840.

14 V. Srinivasan and J. Newman, *J. Electrochem. Soc.*, 2004, **151**, A1517–A1529.

15 B. C. Han, A. V. der Ven, D. Morgan and G. Ceder, *Electrochim. Acta*, 2004, **49**, 4691–4699.

16 G. K. Singh, G. Ceder and M. Z. Bazant, *Electrochim. Acta*, 2008, **53**, 7599–7613.

17 K. E. Thomas-Alyea, *ECS Transactions*, 2008, **16**, 155–165.

18 S. Dargaville and T. W. Farrell, *Electrochim. Acta*, 2013, **94**, 143–158.

19 P. Bai, D. A. Cogswell and M. Z. Bazant, *Nano Lett.*, 2011, **11**, 4890–4896.

20 D. Cogswell and M. Z. Bazant, *ACS Nano*, 2012, **6**, 2215–2225.

21 D. Burch and M. Z. Bazant, *Nano Letters*, 2009, **9**, 3795–3800.

22 M. Tang, H.-Y. Huang, N. Meethong, Y.-H. Kao, W. C. Carter and Y.-M. Chiang, *Chem. Mater.*, 2009, **21**, 1557–1571.

23 J. L. Allen, T. R. Jow and J. Wolfenstine, *J. Solid State Electrochem.*, 2007, **12**, 1031–1033.

24 J. L. Allen, T. R. Jow and J. Wolfenstine, *Chem. Mater.*, 2008, **19**, 2108–2111.

25 G. Oyama, Y. Yamada, R. Natsui, S. Nishimura and A. Yamada, *J. Phys. Chem. C*, 2012, **116**, 7306–7311.

26 M. Farkhondeh and C. Delacourt, *J. Electrochem. Soc.*, 2012, **159**, A177–A192.

27 M. Farkhondeh, M. Safari, M. Pritzker, M. Fowler, T. Han, J. Wang and C. Delacourt, *J. Electrochem. Soc.*, 2014, **161**, A201–A212.

28 G. Chen, X. Song and T. J. Richardson, *Electrochem. Solid State Lett.*, 2006, **9**, A295–A298.

29 L. Laffont, C. Delacourt, P. Gibot, M. Y. Wu, P. Kooyman, C. Masquelier and J.-M. Tarascon, *Chem. Mater.*, 2006, **18**, 5520–5529.

30 S.-I. Nishimura, G. Kobayashi, K. Ohoyama, R. Kanno, M. Yashima and A. Yamada, *Nature Mater.*, 2008, **7**, 707–711.

31 M. Safari, M. Farkhondeh, M. Pritzker, M. Fowler, T. Han and S.-K. Chen, *Electrochim. Acta*, 2014, **115**, 352–357.

32 I. V. Thorat, T. Joshi, K. Zaghib, J. N. Harb and D. R. Wheeler, *J. Electrochem. Soc.*, 2011, **158**, A1185–A1193.

33 C. Delmas, M. Maccario, L. Croguennec, F. L. Cras and F. Weill, *Nature Mater.*, 2008, **7**, 665–671.

34 G. Brunetti, D. Robert, P. Bayle-Guillemaud, J. L. Rouviere, E. F. Rauch, J. F. Martin, J. F. Colin, F. Bertin and C. Cayron, *Chem. Mater.*, 2011, **23**, 4515–4524.

35 W. C. Chueh, F. E. Gabaly, J. D. Sugar, N. C. Bartelt, A. H. McDaniel, K. R. Fenton, K. R. Zavadil, T. Tyliszczak, W. Lai and K. F. McCarty, *Nano Lett.*, 2013, **13**, 866–872.

36 D. Robert, T. Douillard, A. Boulineau, G. Brunetti, P. Nowakowski, D. Venet, P. Bayle-Guillemaud and C. Cayron, *ACS Nano*, 2013, **7**, 10887–10894.

37 W. Dreyer, I. Muller and P. Strehlow, *Q. J. Mech. Appl.*, 1982, **35**, 419.

38 W. Kitsche, I. Muller and P. Strehlow, *IMA*, 1986, **3**, 213.

39 W. Dreyer, J. Jamnik, C. Guhlke, R. Huth, J. Moskon and M. Gaberscek, *Nature Mater.*, 2010, **9**, 448–453.

40 W. Dreyer, C. Guhlke and M. Herrmann, *Continuum Mech. Thermodyn.*, 2011, **23**, 211–231.

41 R. Malik, A. Abdellahi and G. Ceder, *J. Electrochem. Soc.*, 2013, **160**, A3179–A3197.

42 S. Dargaville and T. W. Farrell, *Electrochim. Acta*, 2013, **111**, 474–490.

43 T. R. Ferguson and M. Z. Bazant, *J. Electrochem. Soc.*, 2012, **159**, A1967–A1985.

44 B. Orvananos, R. Malik, H. C. Yu, A. Abdellahi, C. P. Grey, G. Ceder and K. Thornton, *Electrochim. Acta*, 2014, **137**, 245–257.

45 X. Zhang, M. van Hulzen, D. P. Singh, A. Brownrigg, J. P. Wright, N. H. van Dijk and M. Wagemaker, *Nano Lett.*, 2014, **14**, 2279–2285.

46 H. Liu, F. C. Strobridge, O. J. Borkiewicz, K. M. Wiaderek, K. W. Chapman and P. J. C. an C. P. Grey, *Science*, 2014, **344**, 1252817.

47 V. Srinivasan and J. Newman, *Electrochem. Solid State Lett.*, 2006, **9**, A110–A114.

48 T. Sasaki, Y. Ukyo and P. Novak, *Nature Mater.*, 2013, **12**, 569–575.

49 M. Safari and C. Delacourt, *J. Electrochem. Soc.*, 2011, **158**, A63–A73.

50 R. C. smith, *Smart Material Systems: Model Development*, SIAM, Philadelphia, 2005.

51 H. Munakata, B. Takemura, T. Saito and K. Kanamura, *J. Power Sources*, 2012, **217**, 444–448.

52 C. Kuss, D. Lepage, G. Liang and S. B. Schougaard, *Chem. Sci.*, 2013, **4**, 4223–4227.

53 D. Morgan, A. V. der Ven and G. Ceder, *Electrochem. Solid State Lett.*, 2004, **7**, A30–A32.

54 M. Saiful Islam, D. J. Driscoll, C. A. J. Fisher and P. R. Slater, *Chem. Mater.*, 2005, **17**, 5085–5092.

55 Y. Zhu and C. Wang, *J. Power Sources*, 2011, **196**, 1442–1448.

56 C. Delacourt and M. Safari, *Electrochim. Acta*, 2011, **56**, 5222–5229.

57 W. Weppner and R. A. Huggins, *J. Electrochem. Soc.*, 1977, **124**, 1569–1578.

58 A. H. Thompson, *J. Electrochem. Soc.*, 1979, **126**, 608–616.

59 M. D. Levi, S. Sigalov, G. Salitra, P. Nayak and D. Aurbach, *J. Phys. Chem. C*, 2013, **117**, 15505–15514.

60 Y. Orikasa, T. Maeda, Y. Koyama, H. Murayama, K. Fukuda, H. Tanida, H. Arai, E. Matsubara, Y. Uchimoto and Z. Ogumi, *J. Am. Chem. Soc.*, 2013, **135**, 5497–5500.